nature communications

Article

https://doi.org/10.1038/s41467-025-63513-z

Terahertz asynchronous twin-comb for prefiguring hypersensitivity beyond spectrum domain

Received: 10 April 2025

Accepted: 21 August 2025

Published online: 26 September 2025

Check for updates

Liang Ma[1,2], Fei Fan[1,3,4] ✉, Jixin Feng[1,2], Peng Shen[1,3], Chengwei Song[1,2], Yunyun Ji[1,2], Xianghui Wang[1,2] & Shengjiang Chang[2,4] ✉

Lower-frequency characteristics of the terahertz regime confer advantageous low photon energy for biochemical sensing while imposing inherent sensitivity constraints. Here, we demonstrate a terahertz asynchronous twin-comb sensor and an extra-spectrum sensing mechanism through cascading microchannel architecture within a metallic waveguide. The extra-spectrum sensing prefigures an enhanced sensitivity of 4 orders of magnitude compared to existing terahertz biosensing and surpasses its counterpart in the optical band. Hypersensitivities of 0.398 GHz mm^2 pg^{-1} in trace detection manifest through the located characteristic resonance frequency beyond the spectrum domain. Additionally, we observed the photoisomerization of azo dye in the terahertz band with a photoresponse sensitivity of 0.91 GHz cm^2 mW^{-1}, opening possibilities for photoactive material-assisted terahertz sensors. In summary, we instantiate an asynchronous twin-comb sensing beyond the spectrum domain, offering a perspective for ultrasensitive sensing, and promising applications in optical frequency comb precision metrology, artificial intelligence photonics, and integrated sensing and communications.

Terahertz spectroscopy has emerged as a transformative tool for probing collective vibrational modes and rotational states of biomolecules, offering unparalleled insights into molecular dynamics[1–3]. Capitalizing on the merits of label-free detection, rapid response, and on-chip integration, terahertz biosensing has demonstrated remarkable progress in spectral enhancement[4,5], trace analysis[6], and specific sensing[7]. Recent advances utilizing high-Q resonant metamaterials have enabled groundbreaking explorations in life sciences, including amino acids[8], proteins[9,10], cells[11,12], and DNA[13–15]. By integrating functional micro/nanomaterials, biofunctionalization strategies, and artificial intelligence, these advancements have achieved unprecedented sensitivity and detection limits[16,17]. Nevertheless, two intrinsic limitations persist: (1) The dimensional mismatch between analytes and the terahertz wavelength restricts near-field interaction efficiency[18], imposing a sensitivity ceiling; (2) the fixed resonance characteristics of metamaterial-based sensors inherently compromise broadband spectral response, thereby limiting the extraction of multi-dimensional information (frequency shift, amplitude variation, and phase modulation) critical for multiplexed sensing.

To overcome these constraints, waveguide-based terahertz sensors have gained traction by leveraging guided-mode confinement to enhance light-matter interaction[19]. Notably, recent achievements in topologically protected waveguide cavity-based sensors have effectively circumvented the intrinsic limitations of conventional on-chip terahertz biosensors, particularly their small mode confinement volumes and scale-dependent sensitivity to structural imperfections[20]. This breakthrough has demonstrated capabilities in real-time quantitative biosensing of biological analytes while maintaining exceptional robustness against fabrication-induced defects[21]. However, resonant waveguide architectures face an irreconcilable trade-off between

[1]Institute of Modern Optics, Nankai University, Tianjin 300350, China. [2]Tianjin Key Laboratory of Micro-scale Optical Information Science and Technology, Tianjin 300350, China. [3]Tianjin Key Laboratory of Optoelectronic Sensor and Sensing Network Technology, Tianjin 300350, China. [4]Academy for Advanced Interdisciplinary Studies, Nankai University, Tianjin 300071, China. ✉e-mail: fanfei@nankai.edu.cn; sjchang@nankai.edu.cn

operational bandwidth and Q-factor, yielding modest sensitivity of hundreds of GHz RIU^{-1}.

Coherent detection schemes, which have achieved ultra-high sensitivity and broadband response in visible and infrared regimes through interferometric or heterodyne principles[22,23], remain under-explored at the terahertz window due to challenges in waveguide and mode coupling. In our prior work, a dual-channel metallic parallel-plate waveguide interferometer achieved about 1 THz RIU^{-1} sensitivity, yet fabrication and structural constraints hindered further improvement[24]. Subsequent development of a self-referenced Vernier sensor via multi-channel waveguide coupling enhanced sensitivity to 10 THz RIU^{-1}, which is still orders of magnitude below the performance benchmarks presented by optical band counterparts[25,26].

Breaking this sensitivity barrier necessitates a paradigm shift toward multilevel coherent signal architectures and high-dimensional spectral information extraction, both of which demand rigorous control over temporal waveform shaping and spectral coherence. Optical frequency combs, with their dense spectral lines acting as "frequency rulers," present an ideal solution for rich spectral information: Dual-comb systems have revolutionized metrology in high-resolution absorption spectroscopy[27], laser-based light detection and ranging[28], distributed fiber optic sensing[29], and trace detection of biochemical samples through improvements in acquisition rates, precisions, and broad tuning ranges[30]; The recent emergence of topological frequency combs has further revealed applications of strongly driven nested-comb systems in multi-region high-resolution analysis, which provides a perspective for obtaining richer spectral information[31,32]. However, these multiple comb configurations remain confined to the system spectral range, failing to exploit sensing channels beyond the spectrum domain that could transcend the current sensitivity limits.

In this work, we demonstrate a hypersensitive sensing strategy beyond the spectrum domain through the innovative implementation of asynchronous twin-comb spectroscopy instantiated in the terahertz regime. Leveraging optical frequency comb principles, we developed a terahertz asynchronous twin-comb sensor that depends on controlled time defect insertion in temporal periodic signals, inducing frequency comb splitting and twin-comb generation. The cascaded microchannel architecture in metallic waveguides creates characteristic temporal sequences with precision time defect control via microchannel length modulation. Based on the twin-comb spectral periodicity, tracking the twin-comb dual-envelope enables the extraction of high-frequency characteristic resonance and hypersensitivity beyond system spectral range limits. Experimental validation reveals unprecedented sensitivities of 2784.7 THz RIU^{-1} and 0.398 GHz mm^2 pg^{-1}, representing a four-order of magnitude enhancement over existing terahertz biosensing platforms while surpassing optical band sensitivities. Notably, this methodology enables the observation of azo-dyes photoisomerization within the terahertz regime, a photorefraction change of 1% RIU with profound implications for the photoactive materials-assisted terahertz sensor.

Results

Configuration of terahertz twin-comb

Frequency combs exhibit discrete and equidistant spectral lines in the frequency domain, corresponding to periodic pulse sequences in the time domain. Building upon this principle, we instantiate a terahertz asynchronous twin-comb generated through the controlled time defect τ in the pulse sequences. The theory of twin-comb operation is strictly demonstrated in Supplementary Information Part I and Figs. S1 and S2.

Figure 1a elucidates the operational principle of our terahertz asynchronous twin-comb sensor. The sensor-modulated terahertz radiation generates twin-comb spectra at the output, where the inherent asynchronism enables independent extraction of the twin-comb dual-envelope. This distinctive feature provides substantial advantages over conventional frequency dual-comb spectroscopy, particularly in achieving enriched spectral information and ultra-sensitive biochemical sensing. Figure 1c presents the sensor architectural configuration and dimensional parameters. The ridge-loaded metallic parallel-plate waveguide ($d_{gap} = 20$ μm) fabricated from 10 μm-thick polyethylene substrates realizes a cascaded microchannel structure. As illustrated in Fig. 1d, the waveguide channel is divided into four discrete regions by metallic layers (with thicknesses of 5 μm and 6 μm to achieve balanced splitting ratios, and a detailed principle is provided in the Supplementary) on the polyethylene surface, with these regions matching into four parallel transmission channels. These parallel channels exhibit distinct detection times characterized by a terahertz time-domain spectroscopy (THz-TDS) system due to the material-induced additional optical path (OP) difference, which is defined as the OP difference by referencing the OP in air over the same propagation distance, as shown in Fig. 1b, e.

Specifically, Channel-1 comprises solely ambient air, yielding an additional OP of $OP_1 + OP_2 = 0$; Channel-2 contains a polyethylene film-air composite structure with an additional OP designated OP_3; Following an analogous methodology, the additional OP for Channel-3 is derived as OP_4, while Channel-4 exhibits a cumulative OP equivalent to $OP_3 + OP_4$ through polyethylene film superposition. Notably, the temporal separation between Channels 1–2 and Channels 3–4 both depend on OP_3, while the Channels 2–3 interval is governed by $OP_4 - OP_3$. This configuration introduces a critical time defect parameter τ for a twin-comb generation: $\tau = (OP_4 - 2OP_3)/c$, where c means the velocity of light. As demonstrated in Fig. 1e, our experimental implementation achieves $\tau = 0.36$ ps through precise control of waveguide and material geometry, and maintains an operational bandwidth constrained below 1 THz with a 27 dB spectral signal-to-noise ratio, as shown in Fig. S3 in Supplementary Information. Importantly, this configuration allows the identification of characteristic resonance frequencies beyond the spectral domain by tracking dual-envelope signatures within the bandwidth.

As established above, the time defect τ is governed by the additional OP from OP_3 and OP_4, demonstrating that precise modulation of the time defect can be achieved through geometric variation of the polyethylene film relative lengths ($2l_I$ vs. l_{II}). Figure 2a schematically illustrates three configurations of this length-dependent modulation. When l_{II} exceeds $2l_I$, time defect $\tau > 0$ induces single-comb spectral splitting into the twin-comb (a low- and high-frequency comb pair), as shown in Fig. 2b. The phase shift imparted by time defect τ drives an asynchronous transmission modulation between the comb pair, manifesting as an anti-correlated transmission relationship: enhancement in one comb transmission corresponds to suppression in another. The transmission envelopes beyond the system spectral domain are prefigured by constructing envelopes through separate tracking of the low- and high-frequency comb components within the system spectral range. The intersection of the dual-envelope precisely locates the twin-comb characteristic resonance frequency f_{cr}. Notably, the twin-comb pair with $\tau > 0$ exhibits persistent low-frequency comb dominance below the characteristic resonance frequency, while $\tau < 0$ shown in Fig. 2a, c displays an inverted transmission.

Crucially, as l_{II} approaches $2l_I$ and the time defect approximates zero, the subtle phase shift produces a gentle modulation in the twin-comb transmission, resulting in the characteristic resonance frequency located by the spectrally extended envelope intersection far from the system spectral range, as shown in Fig. 2a, d. This mechanism establishes a breakthrough sensing capability beyond the spectral domain: tracking intra-spectrum evolution enables the detection of extra-spectrum resonance shifts induced by structural parameters or analytes, effectively leveraging the sensor high-frequency response channels that conventionally remain unexploited. The evolution of twin-comb spectra and their characteristic resonance frequencies with structural parameters are discussed in detail in Supplementary Information Part III.

https://doi.org/10.1038/s41467-025-63513-z

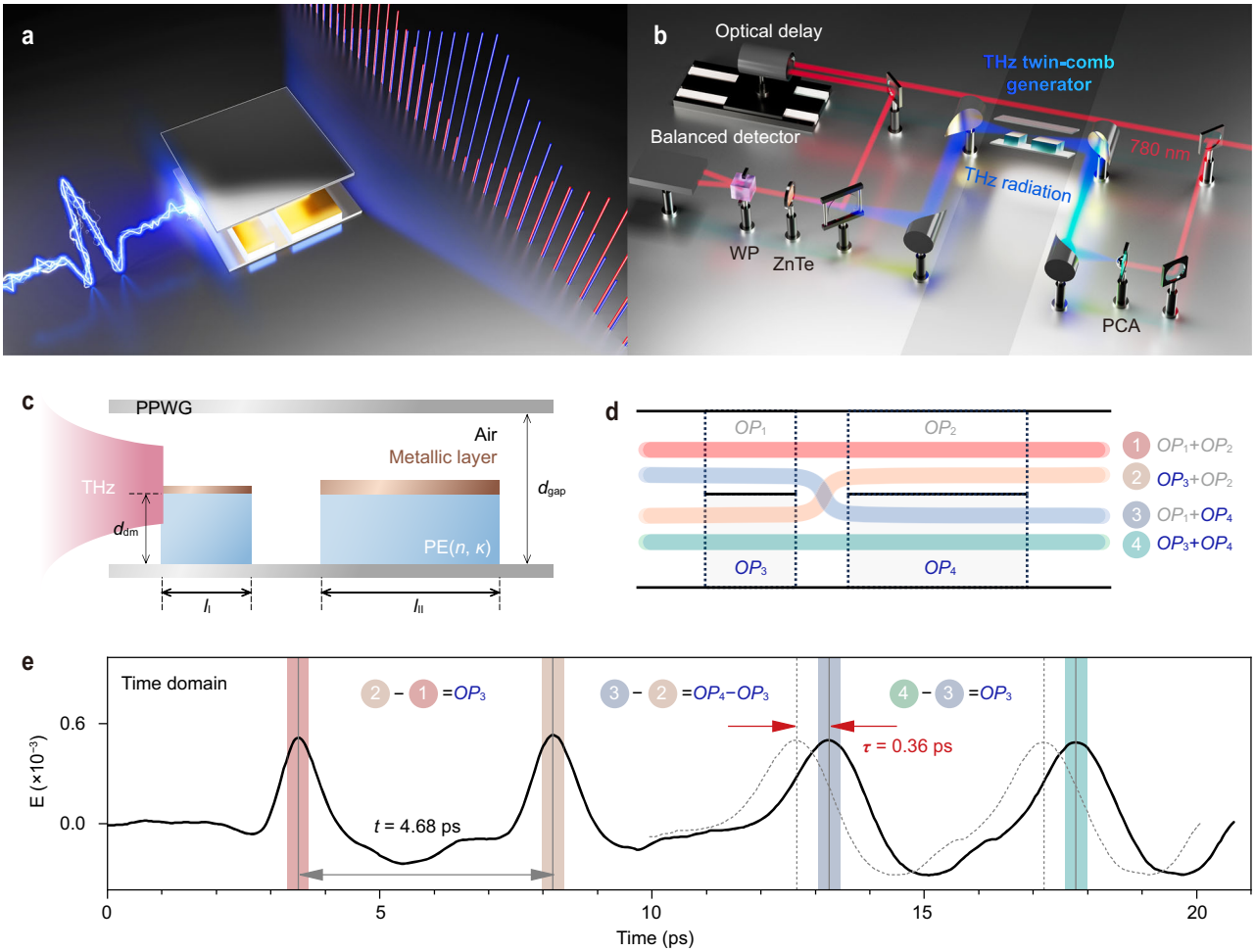

Fig. 1 | Schematic diagram and transmitted characteristics of the terahertz asynchronous twin-comb. a Configuration of a terahertz asynchronous twin-comb. **b** THz-TDS system in experiments. WP Wollaston prism, PCA photoconductive antenna. **c** Two-dimensional diagram and structural parameters of the terahertz asynchronous twin-comb. PPWG parallel-plate waveguide, PE polyethylene. **d** Schematic of the four-channel transmission from a cascading dual microchannel. OP means the additional optical path from materials. **e** Characteristic time-domain series of the terahertz asynchronous twin-comb. Strips with different colors represent the four-channel paths and their transmitted signal. t means the periodic pulse temporal interval. τ means the time defect in the periodic pulse.

Hypersensitivity application

The characteristic resonance frequency f_{cr} of the twin-comb system strongly depends on structural geometry parameters. Analogously, minute variations in microchannel samples also modulate the time defect, generating shifts in the characteristic resonance frequency. This physical mechanism enables the terahertz twin-comb sensors to have exceptional sensitivity beyond the spectral domain.

Figure 3a illustrates the sensing configuration ($l_I = 2.5$ mm and $l_{II} = 5.05$ mm) for quantitative analyte detection, where the sample positioned above the metallic layer introduces additional OP variation OP_2 to modulate the time defect to $\tau = (OP_4 - 2OP_3 - OP_2)/c$. The sensitivity demonstrates substantial fluctuation depending on the effective volumetric ratio η of the samples within the sensing region, as mathematically described by

$$S = \frac{df_{cr}}{dn_s} = \left(m - \frac{1}{2}\right)\frac{l_{II}\eta n_s}{\tau^2 c n_{eff}} \quad (1)$$

where n_s is the refractive index of the sample, and n_{eff} is the equivalent refractive index of the sensing region obtained from the effective medium theory $n_{eff}^2 = n_r^2(1-\eta) + n_s^2\eta$ with $n_r = 1$ showing the refractive index of air[33]. Figure 3b presents the η-dependent sensitivity profile, revealing two critical aspects: Primarily, it reveals the positive correlation between the volumetric ratios of samples in the sensing region and the resulting sensitivity enhancement. Additionally, maintaining a constant sample load while reducing metallic waveguide gaps effectively improves sensitivity optimization. At full volumetric ratio $\eta = 1$, the explicit sensitivity expression for terahertz twin-comb sensing is formulated in

$$S = \left(m - \frac{1}{2}\right)\frac{l_{II}}{\tau^2 c} \quad (2)$$

The combined analysis of time defects, characteristic resonance frequency, and sensitivity yields the time-frequency-dependent sensitivity mapping in Fig. 3c, which elucidates the deterministic relationship between those three factors. Critical observations emerge: (1) The time defect manifests dual characteristics: mirror symmetry about the $\tau = 0$ and intrinsic periodicity synchronized with the periodic pulse temporal interval t. These constraints enforce the bound condition $|\tau| \le t/2$, which governs the cutoff characteristic resonance frequency through the relationship $f_c = m/t$ in different orders; (2) Reduced time defects correlate with elevated characteristic resonance frequencies and enhanced sensitivity; (3) Higher-order characteristic resonance frequencies demonstrate superior sensitivity at equivalent time

https://doi.org/10.1038/s41467-025-63513-z

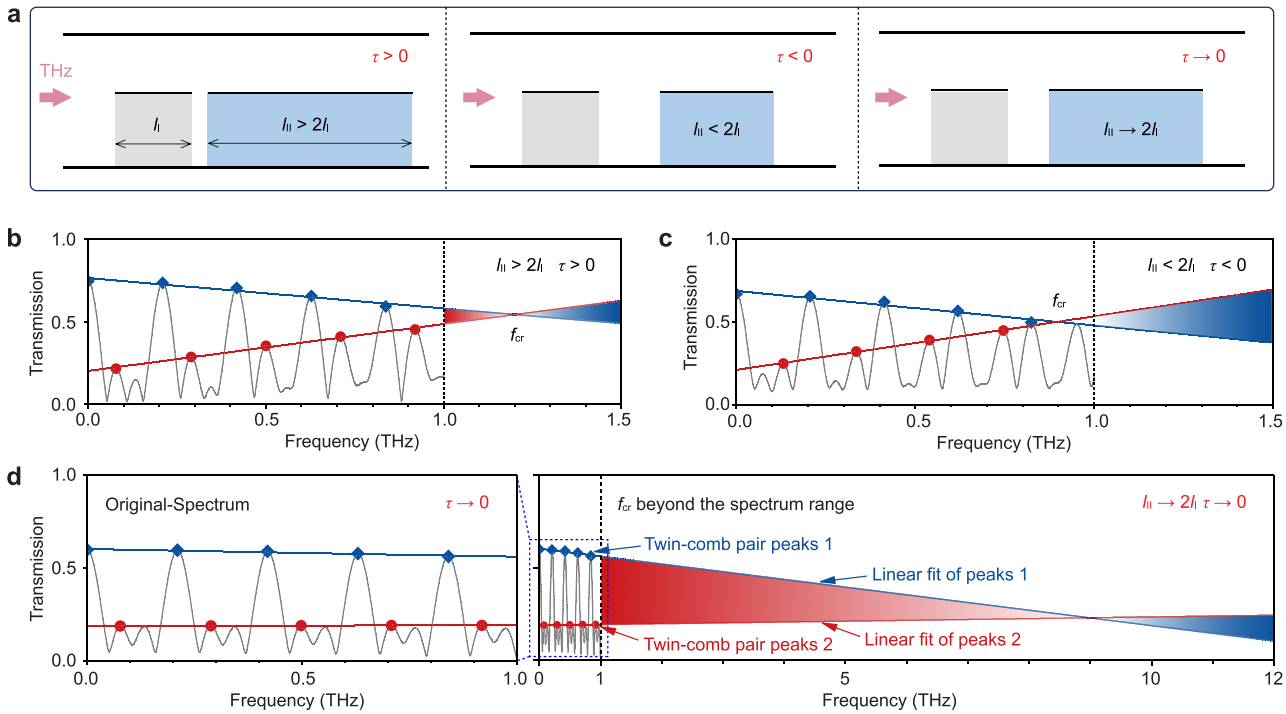

Fig. 2 | Modulation on twin-comb spectra by geometry parameters. a Schematic diagram of the relative geometry of polyethylene films. The gray and blue rectangular elements in the schematic correspond to two polyethylene films with differential transmitted lengths of l_I and l_{II}. Characteristic spectra of the designed terahertz asynchronous twin-comb sensor corresponding to **b** the time defect $\tau > 0$ and **c** the time defect $\tau < 0$. **d** Twin-comb characteristic spectrum with the time defect approaching zero. The blue and red lines represent the dual envelopes obtained by the linear fitting of the twin comb peaks, respectively, and the intersection of the dual-envelope represents the characteristic resonance frequency f_{cr} of the twin-comb. The red-blue gradient background indicates transmission inversion of the twin-comb dual-envelope.

defects as seen $\tau = 0.4$ ps isochron; (4) Lower-order resonances exhibit sensitivity advantages at identical characteristic resonance frequencies as shown $f_{cr} = 10$ THz isoline. These findings establish a design principle: the maximum sensitivity is achieved when the fundamental resonance frequency aligns with the highest utilizable frequency band. The expression for sensitivity is detailedly explained in the Supplementary Information Part II.

Following this principle, Fig. 3d demonstrates the first-order characteristic resonance response near 10 THz for analyte detection. The full volumetric ratio $\eta = 1$ is set in the simulations, indicating complete filling of the sensing region. This configuration establishes the analyte loading profile with a length matching the polyethylene film dimension l_{II} (5.05 mm) and a thickness equivalent to the gap in region two (4 μm) in the *yz* plane. The characteristic resonance frequency contour beyond the spectral range in Fig. 3e quantifies the extra-spectral sensing performance, revealing an unprecedented sensitivity of 2784.7 THz RIU^{-1}. This represents a four-order-of-magnitude enhancement over conventional terahertz biosensors and showcases a significant superiority than optical-band sensing performance.

The exceptional sensitivity of terahertz asynchronous twin-comb sensing was experimentally validated through biochemical sample trace characterization. By leveraging extra-spectral high-frequency sensing channels inherent to the twin-comb configuration, the sensor achieves remarkable detection capability for trace biochemical analytes. Figure 4a demonstrates the sensor response to varying lactose areic masses. Through dual-envelope tracking within the system spectral range, we precisely resolved the characteristic resonance frequency near 10 THz beyond the spectrum domain, revealing significant frequency shifts corresponding to different sample loadings. Subsequent analysis of extra-spectral dual-envelope transmission differences yields the characteristic resonance contour shown in Fig. 4b (Complete spectra seen in Supplementary Information Part IV). With lactose concentration increments set at 1 μg ml^{-1} in a 10 μl solution, the corresponding volumetric increment was calculated as 5.6×10^3 μm^3 under a lactose density of 1.8 g cm^{-3}, which represents a 0.93×10^{-4} fractional volume increase within a 6×10^7 μm^3 sensing region. Hence, the effective medium theory proves an effective refractive index variation of 0.5×10^{-4} RIU with $\eta = 1$, which corresponds to the simulation results in Fig. 3.

A progressive blueshift of 813 GHz was observed as lactose areic masses increased from 0 to 2 ng mm^{-2} in 0.4 ng mm^{-2} increments, shown in Fig. 4c. This phenomenon originates from time defect reduction induced by augmented sample amounts. Linear fit analysis established a sensitivity of 398 GHz mm^2 ng^{-1} with a coefficient of determination $R^2 = 0.97$. The 2.5 pg mm^{-2} detection accuracy is obtained from $\Delta f/S$, where $\Delta f = 1$ GHz means the spectral resolution, confirming superior quantitative performance. Comparative studies in Fig. 4d with conventional terahertz Mach–Zehnder interferometric sensors formed by a single polyethylene substrate in the parallel-plate waveguide reveal limitations in trace detection within the 1 THz operational range.

The breakthrough sensitivity enhancement is quantitatively illustrated in Fig. 4e by comparing against existing typical terahertz and optical sensing mechanisms[8,24,26,34–54]. The extra-spectral sensing mechanism of the twin-comb configuration enables operational frequencies beyond the spectral domain, demonstrating sensitivities that surpass traditional counterparts in the terahertz regime by four orders of magnitude, while outperforming optical-band sensors in sensitivity metrics. This advancement effectively circumvents the conventional low-frequency constraints of terahertz sensing, establishing a paradigm for ultrasensitive biochemical detection in the terahertz regime.

Observation of photoisomerization

Photoresponsive materials, such as azo derivatives exhibit unique light-manipulable properties through photochromic functionality[55,56]. The mechanism involves reversible trans-cis photoisomerization

https://doi.org/10.1038/s41467-025-63513-z

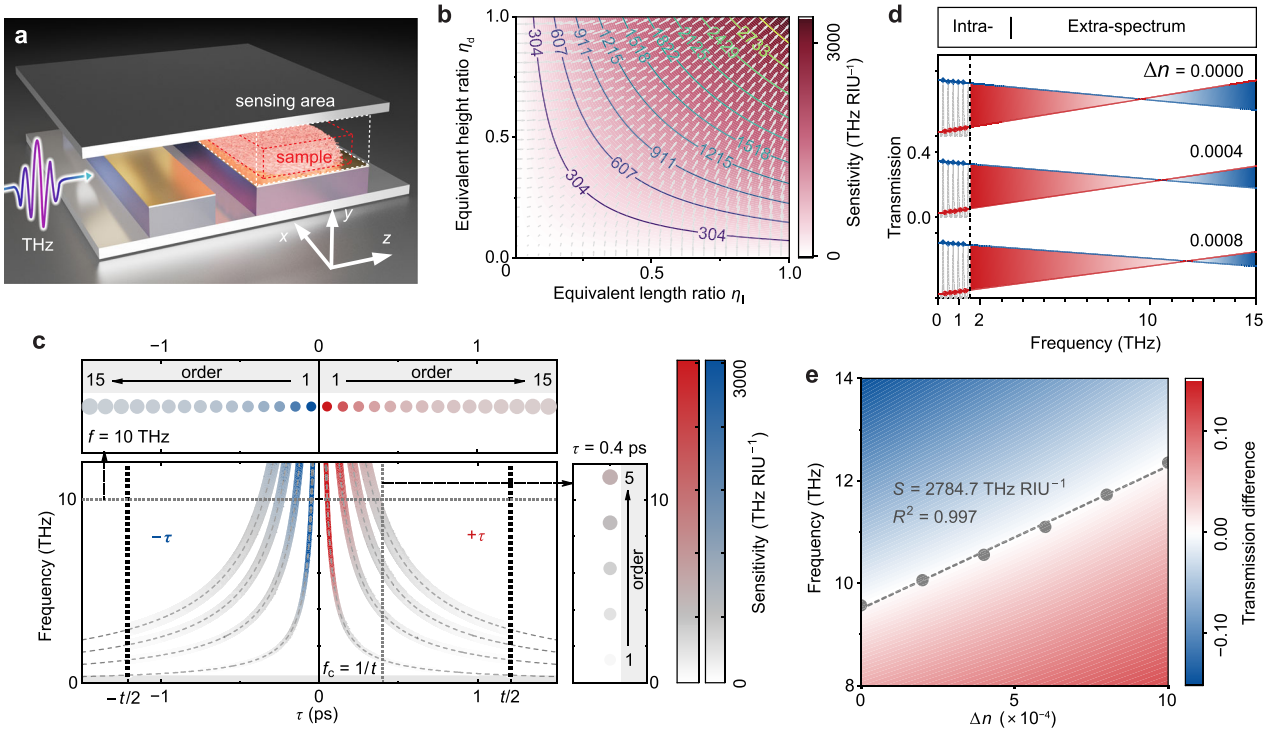

Fig. 3 | Numerical analysis of terahertz asynchronous twin-comb sensing applications. a Sensing diagram. The white and red dashed areas represent the equivalent volume of the sensing region and sample. **b** Terahertz twin-comb sensitivity curves related to the sample spatial proportion. The color lines represent the sensitivity contours. η_l and η_d represent the normalized length and height proportion of the sample within the *yz*-plane of the sensing area in (**a**). The white rows are the gradient of sensitivity. **c** The twin-comb sensor time-frequency dependent sensitivity curves in different characteristic resonance frequency orders. Saturation represents sensitivity. Wider stripes represent higher-order characteristic resonance frequencies. **d** The twin-comb spectral response to the refractive index of the sample. Δn means the change in refractive index of the sample. **e** Contour of characteristic resonance frequency corresponding to different sample refractive index. The red-white-blue gradient contour means the transmission difference in the twin-comb dual-envelope. *S* indicates the sensing sensitivity. R^2 represents the coefficient of determination.

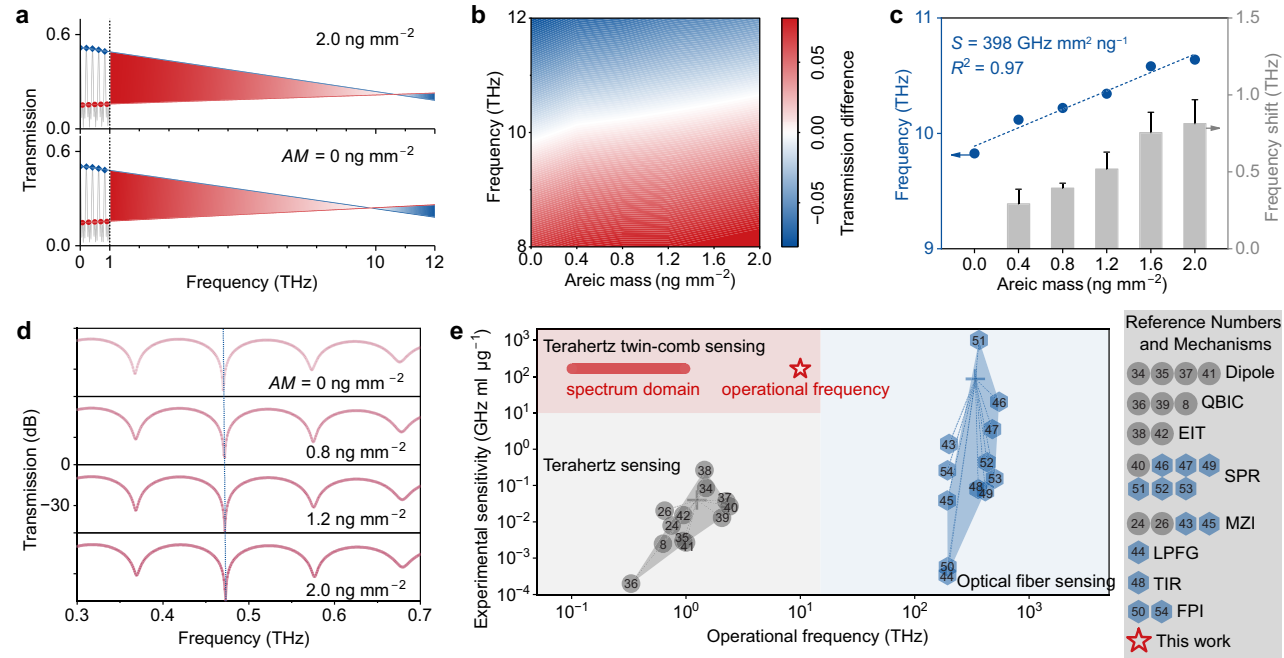

Fig. 4 | Experimental sensitivity characterization of the terahertz asynchronous twin-comb sensor. a The measured transmission spectra and characteristic resonance frequency response with different lactose areic masses. AM areic mass. **b** Contour of characteristic resonance frequency corresponding to different lactose areic masses with an interval of 0.4 ng mm^{-2}. **c** Linear fit of the characteristic resonance frequencies and the response of the frequency shifts in (**b**). Error bars indicate the standard deviation of 5 independent replicates. **d** Response of the terahertz Mach–Zehnder interferometer sensor to different lactose areic masses for sensing performance comparison. **e** Comparisons between terahertz asynchronous twin-comb sensors and existing terahertz/optical-band biochemical sensors from the two dimensions of operational frequency and experimental sensitivity. QBIC quasi-bound states in the continuum, EIT electromagnetically induced transparency, SPR surface plasmon resonance, MZI Mach–Zehnder interferometer, LPFG long-period fiber grating, TIR total internal reflection, FPI Fabry-Pérot interferometer.

https://doi.org/10.1038/s41467-025-63513-z

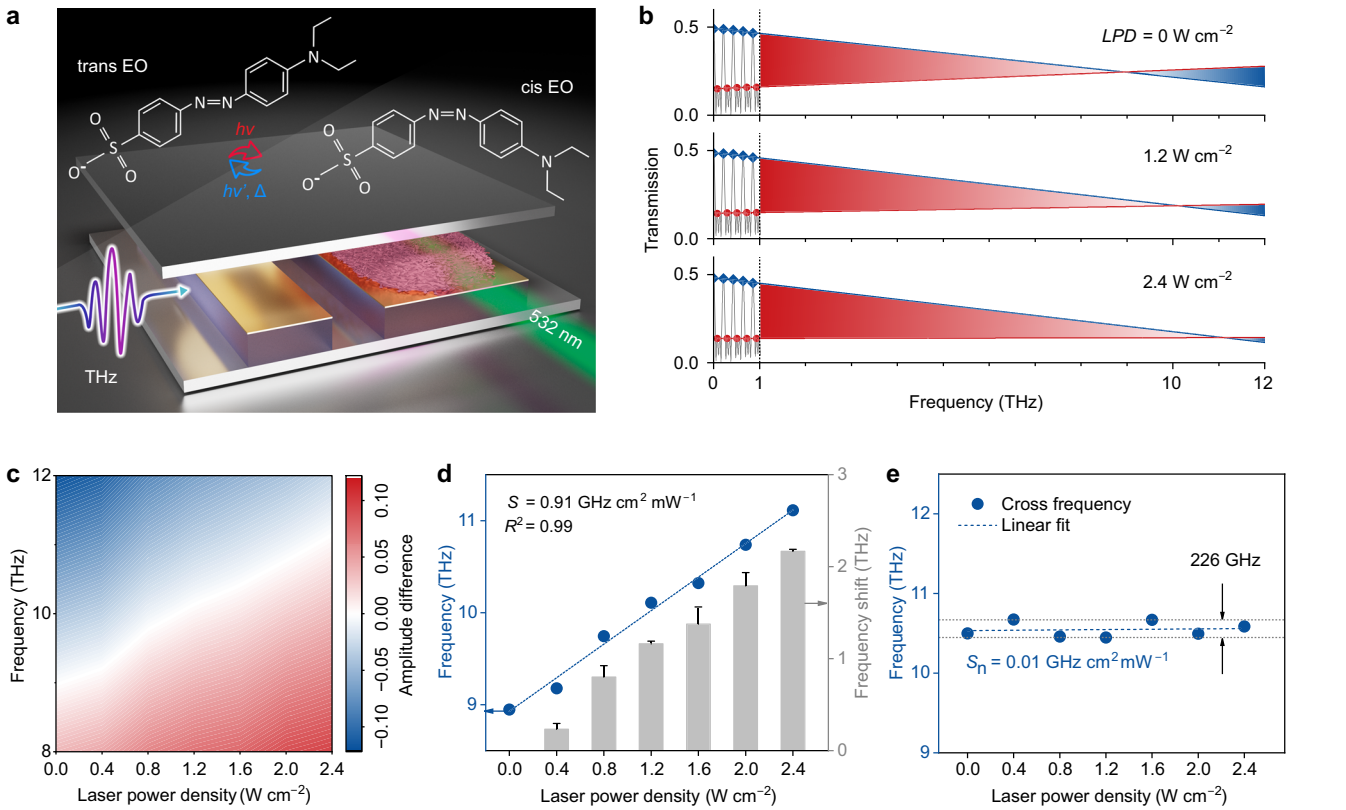

Fig. 5 | The observation of azo dye photoisomerization in the terahertz band. **a** The ethyl orange-loaded terahertz asynchronous twin-comb sensing configuration. EO ethyl orange. **b** The measured transmission spectra and characteristic resonance frequency response of the proposed sensor with different laser power densities. LPD laser power density. **c** Contour of the twin-comb dual-envelope transmission difference corresponding to different laser power densities with an interval of 0.4 W cm^{-2}. **d** Linear fit analysis of the characteristic resonance frequencies and the response of the frequency shifts to laser power densities. Error bars indicate the standard deviation of 5 independent replicates. **e** Comparison in the response of the characteristic resonant frequency of the twin-comb sensor without an ethyl orange load to the laser power densities. S_n means the noise-induced sensitivity error.

under specific wavelength excitation, a phenomenon that has attracted significant interest in optical information storage applications[57,58]. Nevertheless, the development of photoactive terahertz photonic devices remains embryonic, primarily constrained by the weak light-matter interaction at terahertz bands arising from the low-frequency characteristics, which inherently limits material response sensitivity in this spectral regime.

Capitalizing on our proposed asynchronous twin-comb sensing architecture with unprecedented sensitivity beyond the spectral range, the observation of the azo dye photoisomerization is demonstrated in the terahertz bands through the ethyl orange-loaded sensing configuration illustrated in Fig. 5a. Ten microgram ethyl orange with a density of 1.28 g cm^{-3} estimated based on methyl orange analogs due to unavailable reference data, results in an approximate effective volumetric ratio $\eta = 0.13$. Under 532 nm irradiation, the characteristic resonance frequencies in Fig. 5b reveal power-dependent trans-cis isomerization through 2.167 THz blue-shifting behavior over 0–2.4 W cm^{-2} laser power densities, attributed to reduced time defects induced by molecular reconfiguration. The twin-comb dual-envelope transmission difference contour shown in Fig. 5c quantifies this photoresponsive behavior with a 0.4 W cm^{-2} interval (Complete spectra seen in Supplementary Information Part V). Linear regression analysis establishes a remarkable sensitivity of 0.91 GHz cm^2 mW^{-1} with a coefficient of determination $R^2 = 0.99$ shown in Fig. 5d, while comparative measurements without the ethyl orange-loaded sensor in Fig. 5e exclude photothermal effects through slight fluctuation. The noise-induced 226 GHz measurement fluctuations induce a 0.01 GHz cm^2 mW^{-1} sensitivity error in the vicinity of 10 THz, translating to a sensitivity uncertainty of 1.1% in the twin-comb system.

The observation of the azo dye photoisomerization in the terahertz band serves as an instantiation of the ultra-sensitivity of our proposed terahertz twin-comb extra-spectral sensing mechanism and also provides a promising solution for terahertz photoactive materials-assisted sensors.

Discussion

The developed terahertz asynchronous twin-comb and extra-spectrum sensing mechanism overcomes the intrinsic sensitivity limitations imposed by the low-frequency characteristics of the terahertz band. This breakthrough is achieved through four key innovations:

Firstly, the twin-comb spectrum is derived from the inserted time defects in periodic signals. The resultant high-frequency characteristic resonances from subpicosecond-scale time defects permit locating through the twin-comb dual-envelope. Secondly, cascaded microchannel architecture in metallic waveguides generates temporal sequences for terahertz twin-comb, achieving characteristic resonance frequencies near 10 THz that significantly exceed the system spectral range. Thirdly, the extra-spectral sensing mechanism demonstrates unprecedented sensitivity of 2784.7 THz RIU^{-1} and 0.398 GHz mm^2 pg^{-1} with 2.5 pg mm^{-2} detection accuracy. This represents a four-order-of-magnitude improvement over existing terahertz biochemical sensing, surpassing optical-band sensitivity benchmarks. Lastly, the exceptional sensitivity enables the observation of azo dye photoisomerization in the terahertz regime, establishing a generic platform for photoactive materials-functionalized terahertz devices.

This terahertz asynchronous twin-comb strategy provides extra-spectrum sensing paradigms, offering perspectives for potential applications in hypersensitive terahertz biochemical sensing, optical frequency comb metrology, artificial intelligence photonic systems, and integrated communication-sensing technologies.

Methods

Experimental system

The experimental configuration of the transmissive THz-TDS system is presented in Fig. 1b. A femtosecond laser (780 nm central wavelength) is split into two beams. The pump beam is focused onto a photoconductive antenna fabricated from a 50 μm LT-GaAs antenna to generate broadband linearly polarized terahertz pulses. Concurrently, the probe beam undergoes temporal delay modulation before converging with the terahertz radiation on the ZnTe crystal for coherent detection. Terahertz pulses induce birefringence in the ZnTe crystal. Subsequent differential detection using a balanced detector enables precise quantification, with the measured signal amplitude being directly proportional to the instantaneous terahertz field intensity. The implemented THz-TDS system exhibits an operational bandwidth spanning 0.05–1 THz with a signal-to-noise ratio of 10^5 and a spectral resolution of 1 GHz.

Simulation

The spectral results in Fig. S1b, c are derived through numerical implementation of Equation (S5). The simulation results presented in Fig. 3d and Supplementary Information Part III are performed using the commercial Ansys Optics software, incorporating a finite-difference time-domain solver. In our simulation architecture, the perfect electric conductor boundary condition is implemented for the metallic waveguide and metallic layers, while the polyethylene substrate is modeled using a complex refractive index formalism accounting for its dielectric response (a refractive index $n = 1.5$ and an extinction coefficient $\kappa = 0.005$).

Reagent

Lactose solutions with concentrations ranging from 1 to 5 μg ml^{-1} (in 1 μg ml^{-1} increments) are employed for trace biochemical detection experiments. Simultaneously, ethyl orange solutions (1 mg ml^{-1} concentration) are prepared to investigate azo dye photoisomerization phenomena under a precisely controlled 532 nm laser. A 10 μl volume from each concentration is dropped onto a 25 mm^2 effective sensing area and allowed to dry entirely before measurements.

Data availability

All data are available in the main text or the Supplementary Information. Source data are provided with this paper.

References

1. Zunzunegui-Bru, E. et al. Universality in the structure and dynamics of water under lipidic mesophase soft nanoconfinement. *ACS Nano* **18**, 21376–21387 (2024).
2. Zhong, Y. et al. Terahertz photons promote neuron growth and synapse formation through cAMP signaling pathway. *PhotoniX* **6**, 9 (2025).
3. Li, X. J. et al. Terahertz wave desensitizes ferroptosis by inhibiting the binding of ferric ions to the transferrin. *ACS Nano* **19**, 6876–6889 (2025).
4. Lv, J. M., Shen, S. Y., Chen, L., Zhu, Y. M. & Zhuang, S. L. Frequency selective fingerprint sensor: the terahertz unity platform for broadband chiral enantiomers multiplexed signals and narrowband molecular AIT enhancement *PhotoniX* **4**, 28 (2023).
5. Wang, R. D. et al. Multifunctional terahertz biodetection enabled by resonant metasurfaces. *Adv. Mater.* **37**, 12 (2025).
6. Yin, J. F., Chang, H., Geng, W. H. & Xie, L. J. Terahertz SWNT-based fluidic chip for sensing enantioselectivity. *Carbon* **225**, 119116 (2024).
7. Yang, C. et al. Terahertz molecular vibrational sensing using 3D printed anapole meta-biosensor. *Biosens. Bioelectron.* **278**, 117351 (2025).
8. Lin, T. L. et al. Passive trapping of biomolecules in hotspots with all-dielectric terahertz metamaterials. *Biosens. Bioelectron.* **251**, 116126 (2024).
9. Bi, H. et al. A magnetic control enrichment technique combined with terahertz metamaterial biosensor for detecting SARS-CoV-2 spike protein. *Biosens. Bioelectron.* **243**, 115763 (2024).
10. Feng, J. X. et al. Asymmetric dumbbell dimers simultaneously supporting quasi-bound states in continuum and anapole modes for terahertz biosensing. *Nanophotonics* **13**, 4007–4017 (2024).
11. Zhang, C. B. et al. Terahertz meta-biosensor based on high-Q electrical resonance enhanced by the interference of toroidal dipole. *Biosens. Bioelectron.* **214**, 114493 (2022).
12. Lou, J. et al. Calibration-free, high-precision, and robust terahertz ultrafast metasurfaces for monitoring gastric cancers. *Proc. Natl. Acad. Sci. USA* **119**, e2209218119 (2022).
13. Luo, X. Z. et al. Metal-graphene hybrid terahertz metasurfaces for circulating tumor DNA detection based on dual signal amplification. *ACS Sens.* **9**, 2122–2133 (2024).
14. Shen, P. et al. Ultrasensitive terahertz microfluidic biosensor integrated with tetrahedral DNA nanostructure for specific detection of live cancer cells. *Sens. Actuator B Chem.* **428**, 137252 (2025).
15. Shi, W. N. et al. Terahertz let-7a specific sensing and DNA differentiation enabled by Q-BIC metasurface and phenylboronic acid-gold nanoprobe. *Talanta* **297**, 128577 (2026).
16. Xu, W. D. et al. Pesticide detection with covalent-organic-framework nanofilms at terahertz band. *Biosens. Bioelectron.* **209**, 114274 (2022).
17. Zhang, N. et al. Deep-learning empowered customized chiral metasurface for calibration-free biosensing. *Adv. Mater.* **37**, 2411490 (2025).
18. Liu, B. W., et al. Ultra-wideband terahertz fingerprint enhancement sensing and inversion model supported by single-pixel reconfigurable graphene metasurface. *PhotoniX* **5**, 10 (2024).
19. Yang, Y. H. et al. Terahertz topological photonics for on-chip communication. *Nat. Photonics* **14**, 446–451 (2020).
20. Navaratna, N., Tan, Y. J., Kumar, A., Gupta, M. & Singh, R. On-chip topological THz biosensors. *Appl. Phys. Lett.* **123**, 033705 (2023).
21. Kumar, A. et al. Topological sensor on a silicon chip. *Appl. Phys. Lett.* **121**, 011101 (2022).
22. Pan, X. P. et al. High sensitivity fiber optic strain sensor based on CFBG-FPI and Vernier effect. *J. Lightwave Technol.* **41**, 6831–6837 (2023).
23. Zhang, Z. C. et al. A microfiber biosensor for detection of AKT protein in human embryonic kidney cell lysate based on the Vernier effect. *Chem. Eng. J.* **490**, 151435 (2024).
24. Ma, L. et al. Terahertz on-chip sensor based on Mach–Zehnder waveguide interferometer for selective recognition of reducing drug. *Sens. Actuator A Phys.* **370**, 115282 (2024).
25. Ma, L. et al. Lag-compensated hyperfine terahertz dual-comb interferometer beyond intrinsic resolution and sensitivity. *Laser Photonics Rev.* **19**, 2401784 (2025).
26. Ma, L. et al. Retime-mapping terahertz Vernier biosensor for boosting sensitivity based on self-reference waveguide interferometers. *Fundam. Res.* **5**, 593–601 (2025).
27. Xu, B. X., Wan, Y. Y., Fan, X. Y. & He, Z. Y. Whispering-gallery-mode barcode-based broadband sub-femtometer-resolution spectroscopy with an electro-optic frequency comb. *Adv. Photonics* **6**, 016006 (2024).
28. Chang, B. et al. Dispersive Fourier transform based dual-comb ranging. *Nat. Commun.* **15**, 4990 (2024).

29. Youn, J. H., Song, K. Y., Martin-Lopez, S., Gonzalez-Herraez, M. & Fernández-Ruiz, M. R. Brillouin expanded time-domain analysis based on dual optical frequency combs. *Light Sci. Appl.* **13**, 149 (2024).
30. Zano, E., Khrizman, K., Diakonov, A. & Stern, L. Plasmonic-enhanced multiparameter direct microcomb spectroscopy. *Optica* **11**, 1192–1196 (2024).
31. Mittal, S., Moille, G., Srinivasan, K., Chembo, Y. K. & Hafezi, M. Topological frequency combs and nested temporal solitons. *Nat. Phys.* **17**, 1169–1176 (2021).
32. Flower, C. J. et al. Observation of topological frequency combs. *Science* **384**, 1356–1361 (2024).
33. Hu, P. et al. Global phase diagram of bound states in the continuum. *Optica* **9**, 1353–1361 (2022).
34. Shu, J. Y. et al. Terahertz sensing of L-valine and L-phenylalanine solutions. *Sensors* **24**, 3798 (2024).
35. Wang, Y. E. et al. Using mirror-based terahertz metamaterial sensor to chiral identification and detection of D-/L- serine. *IEEE J. Sel. Top. Quantum Electron.* **30**, 6900107 (2024).
36. Tang, X. et al. Hollow-structured all-silicon terahertz metasurface supporting quasi-bound states in the continuum for refractive index based auramine O concentration sensing. *Photonics Res.* **12**, 1574–1582 (2024).
37. Cai, W. J. et al. High performance of terahertz sensor based on double-split hexagonal ring metamaterial. *IEEE Sens. J.* **23**, 22414–22420 (2023).
38. Luo, D. P. et al. Highly sensitive qualitative and quantitative identification of cashmere and wool based on terahertz electromagnetically induced transparent metasurface biosensor. *Biosensors* **14**, 240 (2024).
39. Liu, B. W. et al. Terahertz ultrasensitive biosensor based on wide-area and intense light-matter interaction supported by QBIC. *Chem. Eng. J.* **462**, 142347 (2023).
40. Sun, H. S. et al. A high-efficiency terahertz sensor based on surface lattice resonance metasurface for biochemical detection. *Sens. Actuator A Phys.* **377**, 115711 (2024).
41. Shi, W. N. et al. Terahertz immunosensing assisted by functionalized Au NPs based on all-dielectric metasurface. *Sens. Actuator B Chem.* **362**, 131777 (2022).
42. Lang, T. T. et al. Bovine serum albumin detection based on electromagnetically induced transparency in terahertz metamaterial. *Sens. Actuator A Phys.* **360**, 114522 (2023).
43. Yang, X. C. et al. Temperature self-compensated biosensor based on no-core-fiber offset microcavity for label-free BSA detection. *IEEE Trans. Instrum. Meas.* **73**, 7005609 (2024).
44. Zhong, J. L. et al. High-sensitivity optical fiber-based glucose sensor using helical intermediate-period fiber grating. *Sensors* **22**, 6824 (2022).
45. Hu, X. G. et al. In-fiber optofluidic Michelson interferometer for detecting small volume and low concentration chemicals with a fiber ring cavity laser. *Sens. Actuator B Chem.* **370**, 132467 (2022).
46. Chou, H. T. et al. Development of localized surface plasmon resonance-based optical fiber biosensor for immunoassay using gold nanoparticles and graphene oxide nanocomposite film. *IEEE Sens. J.* **22**, 6593–6600 (2022).
47. Chou, H. T., Su, W. C., Wu, T. M. & Chen, R. P. Optical fiber-based localized surface plasmon resonance biosensor using gold nanorods encapsulated in graphene oxide nanocomposite film applied for immunoassay. *IEEE Sens. J.* **22**, 23923–23930 (2022).
48. Zhou, C. Q. et al. Ultrasensitive total internal reflection sensor with rotatory biased weak measurement. *Sens. Actuator B Chem.* **377**, 133055 (2023).
49. Wei, Y. et al. Wave type fiber SPR sensor for rapid and highly sensitive detection of hyperoside. *Biomed. Opt. Express* **15**, 3859–3868 (2024).
50. Tabaru, T. E., Karatutlu, A. & Ortaç, B. Phase-shifted Bragg-grating consisting of silicon oxynitride doped silicon and silica alternating layers lab-on-fiber for biosensors with ultrahigh sensitivity and ultralow detection limit. *Opt. Laser Technol.* **167**, 109693 (2023).
51. Li, B. & Wang, Q. Surface electric field enhanced biosensor based on symmetrical U-tapered HCF structure for gastric carcinoma biomarker trace detection. *Biosens. Bioelectron.* **264**, 116666 (2024).
52. Wang, B. T., Niu, Y. X., Zheng, S. W., Yin, Y. H. & Ding, M. An optical fiber immunosensor with a low detection limit based on plasmon coupling enhancement. *J. Lightwave Technol.* **38**, 3781–3788 (2020).
53. Zhang, A. L., Li, Z., Chang, P. X., Shi, Y. M. & Wang, Z. Y. High sensitivity rabbit IgG biosensor co-enhanced by tapered noncore fiber and coupling effect between SPR and LSPR. *Appl. Phys. Lett.* **125**, 193701 (2024).
54. Zhao, Y. et al. Plug-and-play Fabry-Perot interferometric biosensor with Vernier effect for label-free detection of bovine serum albumin. *Sens. Actuator B Chem.* **416**, 135999 (2024).
55. Wang, C. S., Fei, H. S., Qiu, Y., Yang, Y. Q. & Wei, Z. Q. Photoinduced birefringence and reversible optical storage in liquid-crystalline azobenzene side-chain polymers. *Appl. Phys. Lett.* **74**, 19–21 (1999).
56. Liu, H. F. et al. A light-intensity-controlled microfiber-assisted Mach–Zehnder interferometer based on ethyl orange solution under 532 nm laser excitation. *Sens. Actuator B Chem.* **216**, 229–234 (2015).
57. Li, Y. T. et al. Laser-tuned whispering gallery modes in a silica-based microsphere resonator integrated with ethyl-orange-doped polyvinyl alcohol coating. *Sens. Actuator B Chem.* **238**, 98–104 (2017).
58. Xu, Y. H., Chen, X. Y., Zhang, S. J. & Tian, Z. Terahertz biochemical sensor based on multiparameter metasurface for molecular fingerprint detection. *Opt. Laser Technol.* **177**, 110959 (2024).

Acknowledgements

This work was supported by the National Natural Science Foundation of China (62335012 to S.J.C., 62371258 to F.F., 62571272 to Y.Y.J., 62205160 to Y.Y.J., 62435010 to S.J.C.), Natural Science Foundation of Tianjin (24JCYBJC01860 to F.F., 24JCYBJC01750 to Y.Y.J.), Tianjin Youth Science and Technology Talent Project (QN20230227 to F.F.).

Author contributions

L.M. F.F., and S.J.C. conceived the concepts. L.M. J.X.F., and C.W.S. performed the simulations. L.M. F.F., and P.S. conducted the experimental design and data analysis. F.F. S.J.C. Y.Y.J., and X.H.W. polished the language and supervised this work. L.M. and F.F. wrote this paper. All authors discussed the results and commented on the manuscript at all stages.

Competing interests

The authors declare no competing interests.

Additional information

Supplementary information The online version contains Supplementary material available at https://doi.org/10.1038/s41467-025-63513-z.

Correspondence and requests for materials should be addressed to Fei Fan or Shengjiang Chang.

Peer review information *Nature Communications* thanks Chao Chang and the other anonymous reviewer(s) for their contribution to the peer review of this work. A peer review file is available.